The effect of the matrix structure on the metal dusting rate in hydrocarbon environments

by G.A. Slabbert*†‡, F.M.L. Mulaudzi*†‡, L.A. Cornish†‡, M.J. Papo*‡, V. Morudu*, and J. Zhang**

Synopsis

The paper describes work undertaken to identify the influence of the matrix structure on the metal dusting rate of stainless steel alloys. Specifically, the difference in metal dusting rate between austenitic and ferritic stainless steels of similar chromium contents was investigated. The alloys were exposed to metal dusting conditions and their performance compared by weight loss, optical microscopy, scanning electron microscopy, transmission electron microscopy, X-ray diffraction, and Raman spectroscopy. The specific gas mixture used for all the tests were 18.9% CO-79.1% H_2-2% H_2O at 650°C. For austenitic stainless steels, Types 304, 321, 316, and 316Ti were compared to two ferritic grades, namely Types 430 and 441. The resistance of the ferritic grades was found to be significantly better than that of the austenitic grades. This was attributed to greater permeability of chromium through the matrix structure to maintain the protective oxide scale. The results will be used in the development of novel alloys to combat metal dusting.

Keywords
metal dusting, hydrocarbon environments, matrix.

Introduction

Metal dusting, a form of high-temperature corrosion, is a particularly insidious damage mechanism, since when initiated, the metal dusting pit growth rate may reach at least a millimetre per month on stainless steels and an order of magnitude higher on low-alloyed steels (Holland, 2012). It is a widespread problem in the petrochemical industry, particularly in cracker furnaces and reforming units. Other chemical processes where organic compounds are reacting, such as in butane dehydrogenation, acetic acid cracking, and pyridine production, are also subjected to metal dusting. Industrial processes in the heat-treating industry, energy production (coal gasification plants), and ammonia plants are other examples. In recent years, metal dusting has attracted considerable attention due to the development of new processes in the petrochemical industry, as well as in electric power generation. Furthermore, the limitation of the materials of constructions prohibits the use of more energy-favourable processes at higher temperatures.

A definition of metal dusting and the various factors involved in metal dusting were presented by Hochman (1972):

- Environment: gas phase, potentially carburizing and reducing, with or without oxygen
- Temperature: usually 450–800°C.
- Form: localized or general pitting and/or general overall surface wastage; surface usually carburized
- Product: dust or powder composed of graphite mixed with metal, metal carbides, and metal oxides.

The phenomenon of metal dusting may be driven by three main mechanisms, denoted Type I, Type II, and Type III.

Type I, first described by Hochman and Burson (1966) and Hochman (1972), and further detailed by Grabke (1995, 1998), involves decomposition of metastable cementite. Type II may be described as disintegration of a carbon-supersaturated phase by internal graphitization, and was first described by Hultgren and Hillert (1953) and studied in detail by Pippel *et al.* (1995, 1998). Type III, which operates on high-alloyed steels and Ni-

* *Mintek.*
† *University of the Witwatersrand.*
‡ *DST/NRF Centre of Excellence in Strong Materials, hosted by the University of the Witwatersrand, Johannesburg.*
** *School of Materials Science and Engineering, Univeristy of New South Wales.*
 ISSN 2225-6253. This paper was first presented at the, Ferrous and Base Metals Development Network Conference 2012, 15–17 October 2012, Mount Grace Country House and Spa, Magaliesburg, South Africa.

based alloys, was first proposed by Szakálos, Pettersson, and Hertzman (2002), and further described by Szakálos and Liu (2002), and Szakálos (2002; 2003), and involves selective oxidation of alloyed carbides, i.e. not pure Fe-carbides.

A secondary mechanism may be added, namely carbon nanotube formation, Type IV. It may be described as a continued fragmentation of the corrosion products and involves carbon nanotube formation, as was mentioned by Szakálos (2004). There is seldom only one metal dusting mechanism operating on steels or Ni-based alloys. For example, Types III and II operate in conjunction on austenitic stainless steels and Ni-based alloys (Szakálos, 2002, 2003; Szakálos, Pettersson, and Hertzman, 2002; Szakálos and Liu, 2002).

Metal dusting of ferritic chromium steels

The behaviour of ferritic chromium steels exposed to $CO/H_2/H_2O$ gas mixtures depends on whether a chromia scale is formed and retained (Young, 2010). This is similar for the corrosion resistance of stainless steels in aqueous corrosive environments. If the chromium content is too low to form a Cr_2O_3 scale, the steel will dust at the same rate as a low-alloy steel as explained above (for instance a 2¼ Cr-1Mo type alloy). If the steels form a continuous, adherent chromia scale, resistance to dusting under isothermal conditions is very good, because the scale prevents carbon entry. The resistance of an alloy to metal dusting depends on its ability to quickly form a continuous Cr_2O_3 scale by diffusing chromium to the surface (Young, 2010).

The effect of temperature on the diffusion coefficient of chromium (D_{Cr}) was demonstrated by Grabke, Krajak, and Müller-Lorenz (1993). Steels with 17% to 26% chromium showed complete resistance to dusting at 600°C to 650°C, but showed metal dusting attack at 550°C. The susceptibility to dusting therefore increases as the temperature and D_{Cr} decrease. The greater D_{Cr} in ferritic steels ensures that ferritic alloys can heal or repair damaged oxide layers more efficiently than austenitic alloys with a similar chromium content. This leads to improved dusting resistance as shown in Figure 1.

Because the resistance to dusting is increased as D_{Cr} is increased, the effective value for D_{Cr} can be increased at lower temperatures by creating a deformed and fine-grained alloy surface. This is done by surface grinding, shot peening, etc., and has been shown to lead to better dusting resistance (Lai, 2007).

However, alloys that develop continuous protective chromia scales are subject to long-term dusting attack. Under isothermal exposure, growth stress accumulation in the scale eventually leads to mechanical failure. A series of such events can exhaust the capacity of an alloy to heal or regrow its protective scale, and metal dusting follows. Discontinuous exposures and short-term thermal cycling combine the effects of accumulated growth stress and thermal shock. These result in chromium depletion. Further breakdown of the chromia scale allows carbon to enter the chromium-depleted metal (Young, 2010). Rapid inward diffusion of carbon leads to internal precipitation of chromium carbides, thereby preventing subsequent re-healing of the scale.

The depleted iron matrix forms a cementite layer, which disintegrates, producing cementite particles to catalyse further coke deposition – i.e. a similar mechanism to iron and low-alloy steels once the chromium is depleted by being tied-up as internal carbides.

The result is a pitted surface. Continued attack widens the pits and allows them to coalesce, until the attack is eventually general.

If the alloy chromium content is high enough, dusting of ferritics can be prevented (Young, 2010). An Fe-60Cr alloy survived 1000 one hour cycles at 680°C, forming only Cr_2O_3, which was impermeable to carbon. Furthermore, the chromia was catalytically inactive, and no coke deposited.

Metal dusting of higher alloyed steels

The mechanism for metal dusting of nickel alloys differs from that of ferritic material in that cementite is not formed, and the corresponding nickel carbide is unstable. Starting with uncarburized AISI 304L steel, the metal dusting steps were divided into six zones (Szakálos, 2004):

1) Carburized bulk with $M_{23}C_6$ carbides, which forms at lower carbon activities
2) Carburized bulk with M_7C_3 carbides
3) Dissolving carbide front with M_7C_3 and M_3C
4) Cr-depleted zone ('white phase'), Fe-Ni austenite border with graphite flakes
5) Corrosion products: Cr-Fe oxides, metal fragments in micrometre-size, and carbon
6) Coke, continued corrosion of the corrosion products by the Type II mechanism, i.e. disintegration of the metal fragments into smaller and smaller metal dust and finally, nanometre-sized particles, formation of carbon nanotubes.

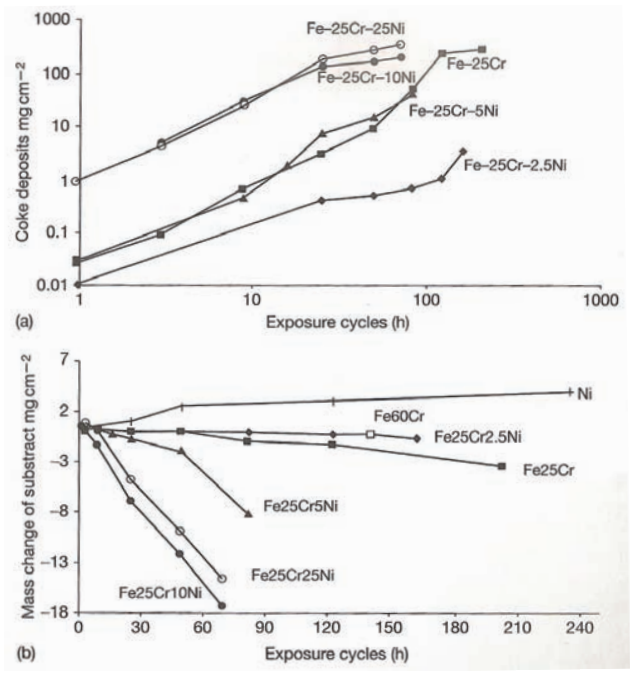

Figure 1—Coke deposition and metal wastage kinetics for electropolished 25Cr alloys at 680°C in $CO/H_2/H_2O$ (Grabke, Krajak, and Müller-Lorenz, 1993)

The process of metal dusting that yields the six zones described above initiates with the selective oxidation of chromium to produce a chromium-depleted subsurface alloy region (Young, 2010). If sufficient chromium remains, the chromia scale re-heals. However, if there is not sufficient chromium to sustain the chromia scale, and the oxygen partial pressure is too low for nickel or iron oxides to form, then carbon enters the alloy to precipitate chromium carbides. At low temperatures, the diffusion coefficient for chromium is small, so the carbides formed are also small. Removal of chromium from the matrix renders future healing of the surface scale impossible, facilitating greater gas entry into the chromium-depleted region. The metal is essentially a Fe-Ni alloy, and at high nickel concentrations, undergoes graphitization and disintegration similarly to pure nickel.

Experimental procedure

Test alloys

The research approach of the project was to expose different stainless steels under a controlled metal dusting environment, to determine how they deteriorated with exposure time. Since the chromium concentration significantly influences the resistance of materials to metal dusting, materials were chosen with an equivalent chromium content, but in different alloys that were either ferritic or austenitic in structure – depending on the nickel content.

Austenitic alloys

- Type 304L stainless steel was used as reference material and its performance compared against that of Type 321 (i.e. essentially Type 304 with Ti added)
- Similarly, the performance of Type 316L stainless steel was compared to that of Type 316Ti (i.e. essentially Type 316 with Ti added). Although the chromium content is generally slightly lower and the nickel content slightly higher in Type 316L compared to Type 304L, the differences are small, which means that the influence of molybdenum can also be assessed by comparing the performance of Type 304L to 316L. Molybdenum is a carbide-former, which is also known to reduce the resistance to metal dusting (Strauss and Grabke, 1998).

Ferritic alloys

- Type 430 stainless steel also has about 18% chromium, similar to the austenitic alloys described above, and was therefore also included in the test programme. Type 430 does not contain any nickel (or other austenite stabilizers) and therefore has a ferritic structure. Comparison between Types 304L and 430 therefore allowed direct assessment of the influence of the matrix structure on the metal dusting rate
- The performance of Type 430 was compared to that of Type 441 (essentially Type 430 with Ti and Nb added – i.e. dual-stabilized grade).

These differences influenced the characteristics of chromium migration and the formation of oxide scales, carbon migration, the formation of carbides and their subsequent oxidation, in the different alloy systems. The chemical compositions of the alloys, as specified in ASTM A240, are listed in Table I.

Sample preparation

All the alloys tested were sourced from Columbus Stainless, and were of similar approximate thickness (2 mm) to ensure that they had been subjected to similar processing conditions during manufacture. All the samples were in the cold-rolled condition. The samples were sectioned into specimens 20 × 20 mm and a 5 mm hole was drilled in the centre to suspend them in the furnace. Although it is known that the surface condition plays a major role in metal dusting resistance, where ground surfaces are more resistant, due to their enabling greater mobility of chromium to repair surface protective scales (Lai, 2007), samples were tested in the ground condition. This was done to closer simulate the condition of material surfaces encountered in practice, to allow a more direct comparison between the different alloys.

The samples were all ground to a 320 grit silicon carbide (SiC) finish. The dimensions of the samples were then measured with a digital calliper to the nearest 0.01 mm and the samples stored in plastic bags. Immediately prior to testing, the samples were degreased with acetone and weighed to the nearest 0.1 mg.

Test procedures

A test rig was purpose-built to control the gas compositions at elevated temperatures in the metal dusting regime. For this, a horizontal ceramic tube furnace was used with Type 316 stainless steel gas pipelines capable of supplying a mixture of gases simultaneously. Mass flow controllers were used to regulate gas flow rates to obtain the desired mixing

Table I

Nominal compositions of the alloys tested (wt%); values indicate maxima unless ranges are specified

	Type 304L	Type 321	Type 316L	Type 316Ti	Type 430	Type 441
C	0.030	0.080	0.030	0.080	0.120	0.030
Cr	17.5-19.5	17.0-19.0	16.0-18.0	16.0-18.0	16.0-18.0	17.5-18.5
Ni	8.0-12.0	9.0-12.0	10.0-14.0	10.0-14.0	0.75	-
Mo	-	-	2.0-3.0	2.0-3.0	-	-
Ti	-	5(C+N) to 0.7	-	5(C+N) to 0.7	-	0.1 to 0.6
Nb	-	-	-	-	-	0.3+3C

ratios. Water vapour was supplied by using a HPLC pump. All the gas tubes passing the water vapour were wrapped with heating tape that was maintained at 120°C.

Three gases were used throughout all the tests performed. Firstly, nitrogen was passed through the furnace once the samples were loaded to flush any oxygen in the system and reduce the oxygen partial pressure. The system was flushed with nitrogen for a minimum of one hour before the temperature was increased to the set temperature. In this study, the temperature was set at 680°C, which yielded an actual temperature in the hot zone of the furnace of 650°C. Once the furnace reached the set temperature, the CO and H_2 flow rates were adjusted using mass flow controllers that regulated the gas mixtures. The gases were mixed, together with the water vapour, and passed through the furnace.

The gas flow rate and temperature were maintained constant throughout the different exposure periods used (i.e. isothermal testing). Although cyclic thermal treatments (intermitted temperatures) speed up the metal dusting process by breaking the protective oxide scale that can cause carbon to diffuse into the metal matrix (Young, 2010), isothermal treatments were used in this study. The breaking of the oxide scale occurs during heating and cooling due to the different expansion coefficients between the matrix and the oxide. The difference between the expansion coefficients for austenite and the oxide scale is larger than that between ferritic materials and the oxide. This is why the recommended service temperatures for intermittent (cyclic) use for ferritic materials are higher than for continuous use, while for austenitics the recommended temperatures for intermittent use is lower than for continuous use (Nickel Development Institute, 2002). Therefore, because austenitic and ferritic materials were tested in this exposure programme, an isothermal regime was used. Furthermore, it was intended to simulate environments in petrochemical plants, where the processes are continuous and not batch processes. The equipment in the plant is therefore not subjected to cyclic temperature conditions that could cause protective oxide scales to crack prematurely, and so the isothermal tests were more realistic.

The specific gas mixture used for all the tests performed was 18.9%CO-79.1% H_2-2%H_2O. At 650°C, the carbon activity for this gas mixture was 11.75 assuming CO + H_2 = H_2O + C was the dominant reaction. The overall flow rate of the gas was 200 mL/minute and the linear gas flow rate in the reactor at 650°C was 4.4 cm/min. Tests were performed for three different time periods; seven days, fourteen days, and thirty days.

Methods of analysis

The following methods were used to evaluate the samples subsequent to testing:

- Visual examination and photographic record
- Weight change to assess coking and metal wastage
- Optical microscopy of each alloy in both the etched and unetched condition. Cross-sections were copper-plated to retain products on the surface and for edge retention during polishing
- Scanning electron microscopy (SEM) with energy-dispersive X-ray spectroscopy (EDX) of the surface and cross-sections
- Transmission electron microscopy (TEM) with energy-dispersive X-ray spectroscopy (EDX) of the coke.

Results

Figure 2 shows the samples as removed from the furnace after the seven-day test, illustrating how they were suspended in the furnace. Some coke formation was evident, particularly associated with the austenitic samples. Figure 3 was taken after the fourteen-day exposure period. Significantly more coke formed during the additional seven days compared to the seven-day test. Most of the coke formation was associated with the austenitic samples. Figure 4 shows the samples after removal from the furnace after the thirty-day test. The coke formation was extensive, and none of the austenitic samples were visible. The ferritic samples also formed coke, but to a lesser degree than the austenitic samples.

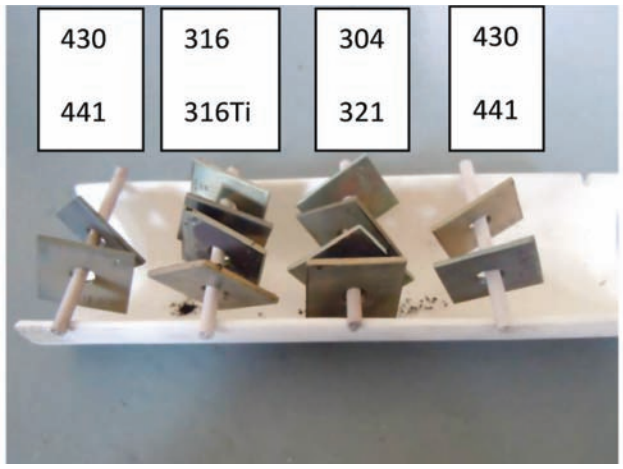

Figure 2—Photograph showing the samples and coking after exposure for 7 days

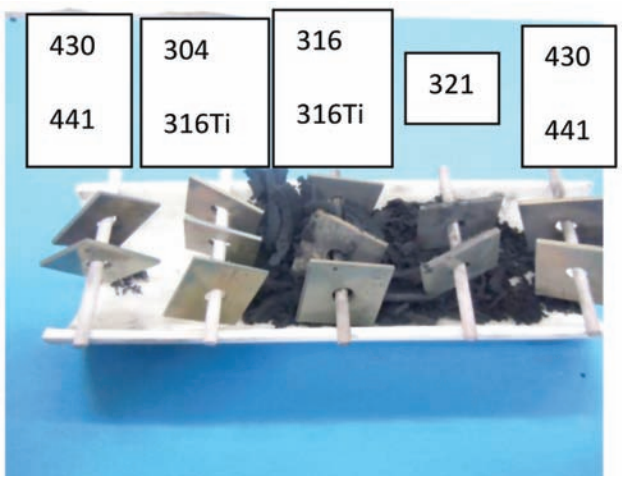

Figure 3—Photograph showing the samples and coking after exposure for 14 days

Figure 4—Photograph showing the samples and coking after exposure for 30 days

Figure 5—Photograph of Type 316L (upper row) and 316Ti samples (lower row) after exposure for 30 days. The samples on the left-hand side were cleaned

No significant attack was evident on the Type 304L or 321 samples after seven days. Figure 5 shows the Type 316L and 316Ti samples after the 30 day test, showing significant metal wastage associated with the coking. Although the attack was by pitting, the pits had grown together to result in uniform metal wastage. Figure 6 compares Type 430 and 441 samples after 30 days, showing products on the surface of the Type 441 that could not be removed after cleaning. Pitting was evident on both alloys, but was significantly less than for Type 316L and 316Ti samples.

The surfaces of the samples were also analysed by SEM. The darker patches associated with the tarnishing on the materials were generally rougher, with associated pitting, compared to the lighter areas. A dark area on the Type 304L sample after the 7 day test exhibiting the initiation of pitting is shown in Figure 7. A fine needle-like phase was also evident, but was too fine to analyse by EDX. Figure 8 shows

Figure 6—Photograph of Type 430 (upper row) and 441 samples (lower row) after exposure for 30 days. The samples on the left-hand side were cleaned

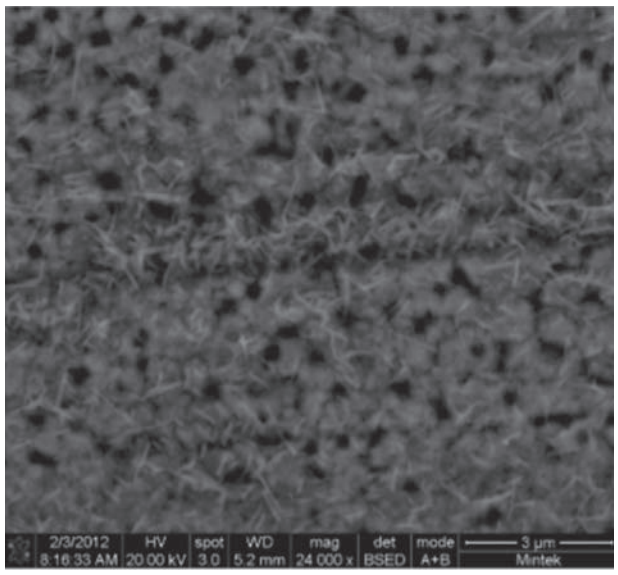

Figure 7—SEM-BSE image of the surface of the Type 304L sample exposed for 7 days

a hemispherical pit that propagated in the 316L sample exposed for seven days. Figure 9 is a section through a pit in the 316L sample exposed for seven days, showing the intergranular nature of the attack and associated carburization. Some intergranular attack was also found on the 316Ti surface. No significant attack was evident on the Type 430 or 441 samples exposed for seven days.

Figure 10 shows the pitting on the Type 316L sample, with multiple pits and the intergranular nature of the attack inside the pits. Figure 11 is a pit in the Type 430 sample showing intergranular attack, and Figure 12 indicates the general surface appearance.

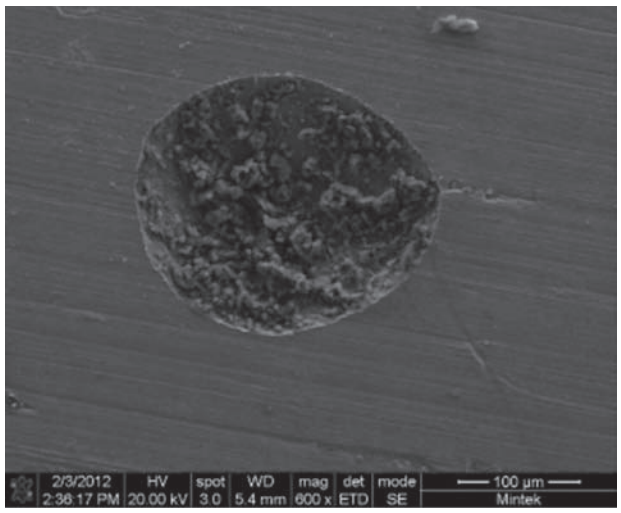

Figure 8—SEM-BSE image of the surface of the Type 316L sample exposed for 7 days

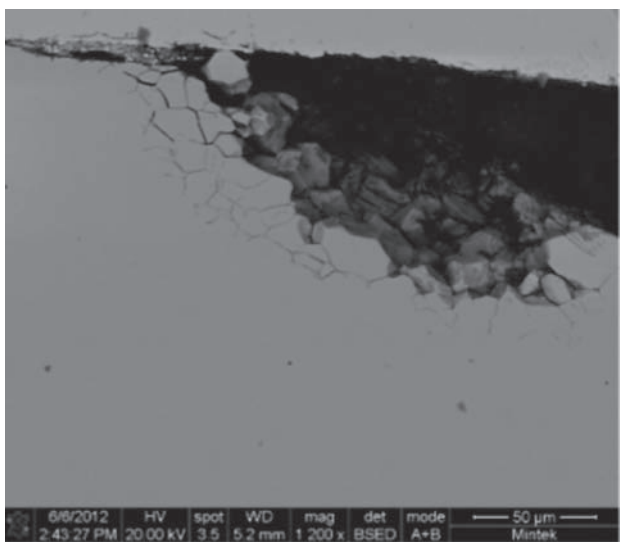

Figure 9—SEM-BSE image of a cross-section from the Type 316L sample exposed for 7 days

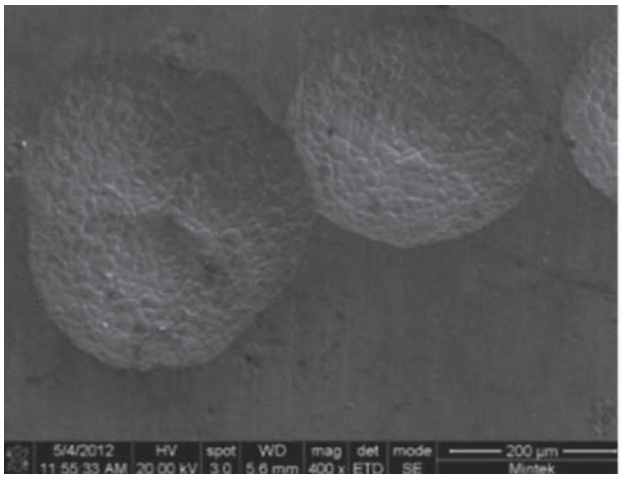

Figure 10—SEM-BSE image of the surface of the Type 316L sample exposed for 30 days

Figure 13 is a cross-section through a Type 304L sample that was exposed for 30 days, and Figure 14 is an EDX line scan taken as illustrated in Figure 13. An oxide layer was visible on the outside surface, which consisted predominantly of chromium and was probably Cr_2O_3. There was also a metallic layer underneath the oxide that could be an iron and/or chromium carbide, but this was not proven because its fineness. Individual round particles were evident below this layer. The chromium-enriched layer was less than 2 µm thick. The composition was relatively constant further in, indicating that the material near the surface was not significantly enriched or depleted in any elements.

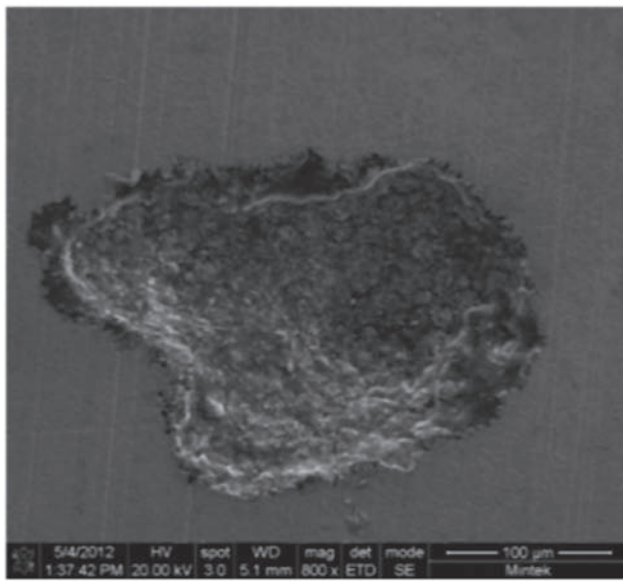

Figure 11—SEM-BSE image of the surface of the Type 430 sample exposed for 30 days

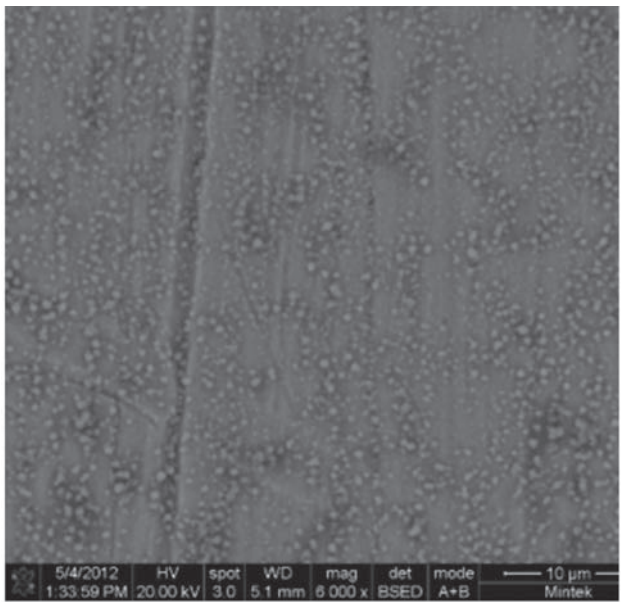

Figure 12—SEM-BSE image of the surface of the Type 430 sample exposed for 30 days

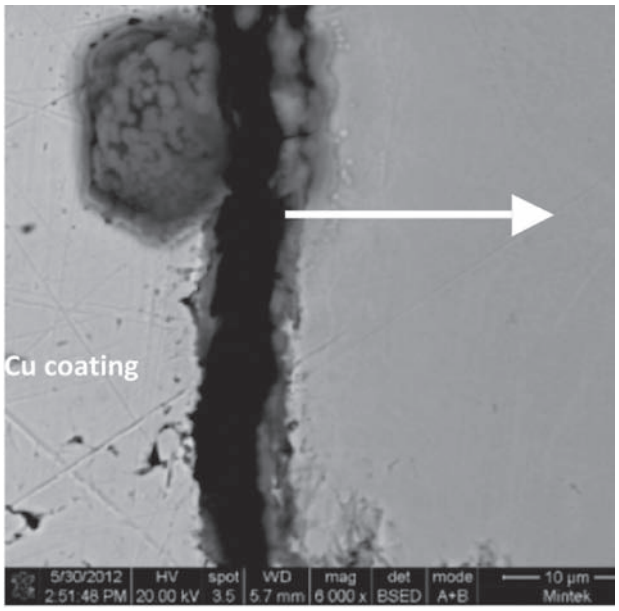

Figure 13—SEM-BSE image of a cross-section through the Type 304L sample

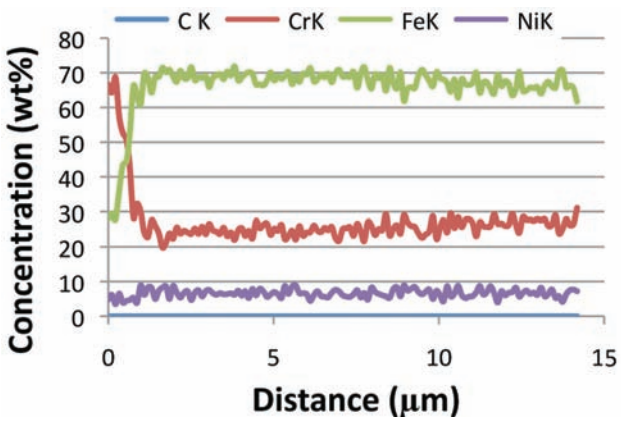

Figure 14—EDX line scan taken as shown in Figure 13

Figure 15 shows intergranular attack in the Type 316L sample exposed for 30 days. Carbides precipitated on the grain boundaries, which were enriched with chromium and molybdenum. Figure 16 shows an EDX line scan through this area illustrating how the composition changes. The molybdenum (together with the chromium) increased from 2% to about 10% on the grain boundary.

Figure 17 is an SEM-BSE image of a cross-section through an area in the Type 430 sample that showed local breakdown in the oxide scale and subsequent carburization. Figure 18 is an EDX line scan through the carburized zone as indicated in Figure 17. The outside layer was scale, consisting of approximate equal quantities of chromium, iron, and oxygen. The decarburized layer essentially consisted only of iron, indicating that most of the chromium had diffused to the surface to repair the oxide and resulted in the material subsurface becoming only carbon steel. Subsequent metal wastage was associated with the region.

Figure 19 and Figure 20 show the coke on the samples, indicating that it consisted of filaments with metallic particles at the tips. Since the samples were tested together, it could not be confirmed from which alloy the metal particles originated, but was likely to be from the Type 316L samples. It could not be conclusively proven whether the particles were pure iron, austenite, or carbides. Figure 21 is a TEM image of the filaments showing that they were hollow tubes. Raman spectroscopy showed that the filaments were multi-walled carbon nanotubes (MWCNTs). The different layers in the wall were also evident in the TEM image.

After the coupons had been cleaned under running water with a soft bristle brush, the corrosion rates were calculated based on the mass-loss incurred (expressed in penetration rate in millimetres per year), as shown in Figure 22. The conversion from mass loss to penetration rate (millimetres per year) was made by assuming uniform mass loss over the

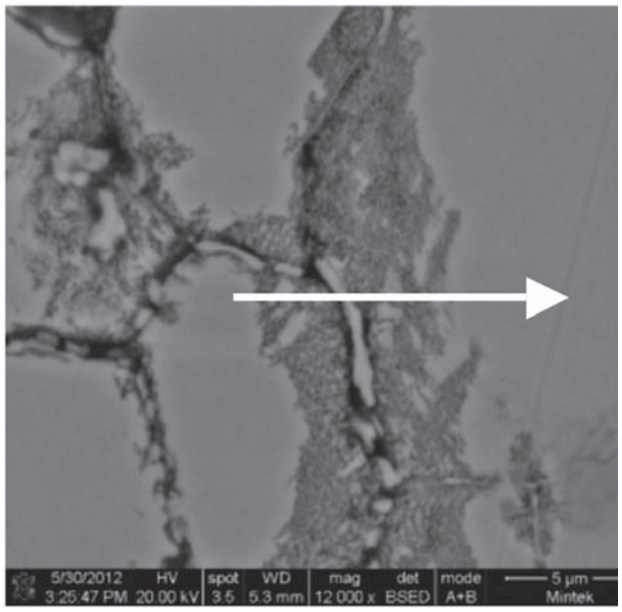

Figure 15—SEM-BSE image of a cross-section through the Type 316L sample

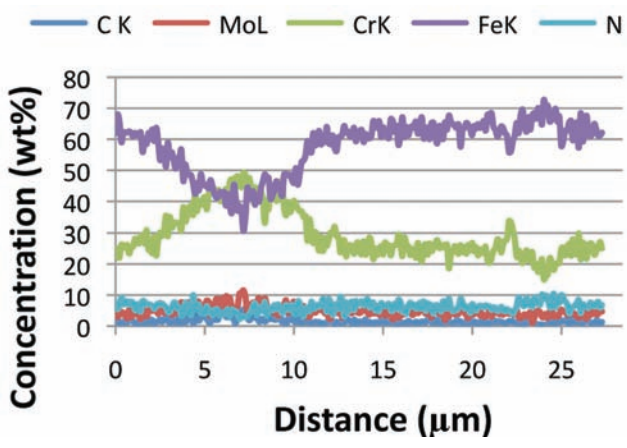

Figure 16—EDX line scan taken as shown in Figure 15

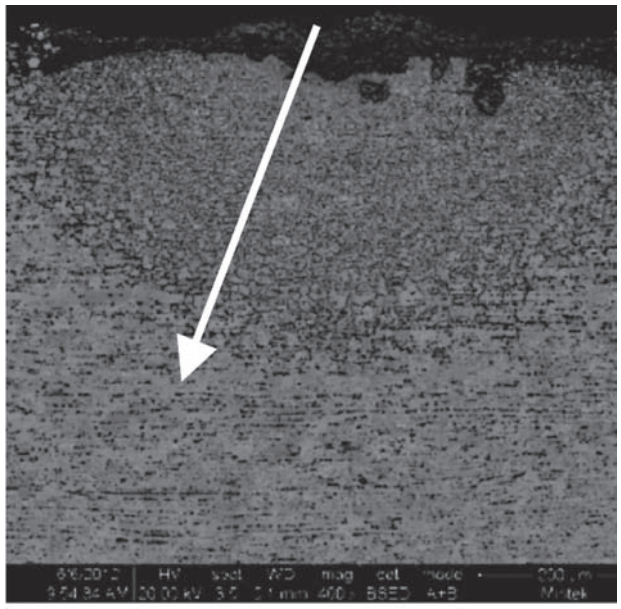

Figure 17—SEM image of a cross-section through the Type 430 sample

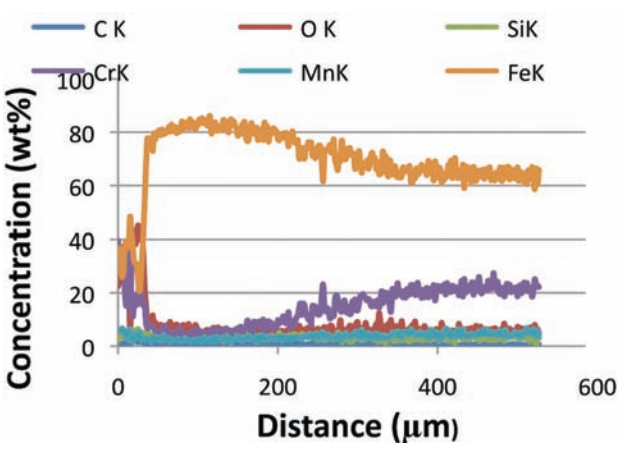

Figure 18—EDX line scan taken as shown in Figure 17

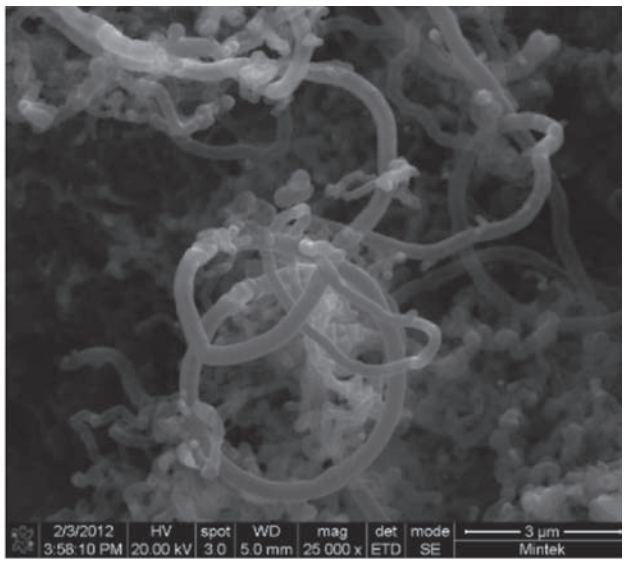

Figure 19—SEM-BSE image of the filaments

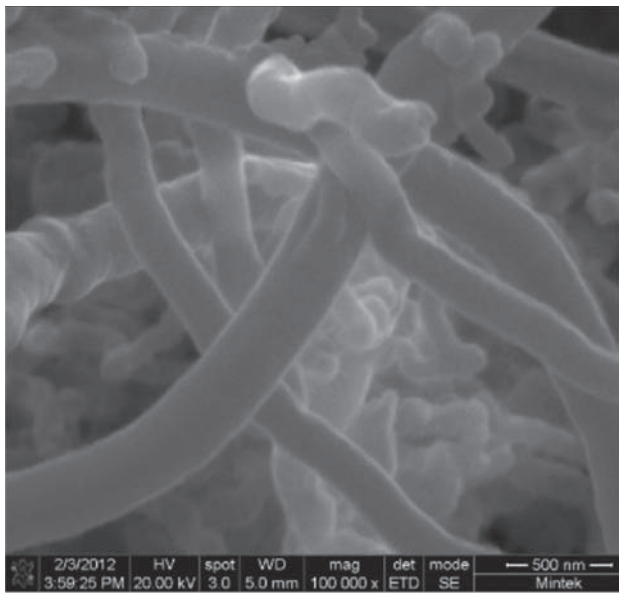

Figure 20—Higher magnification of the coking

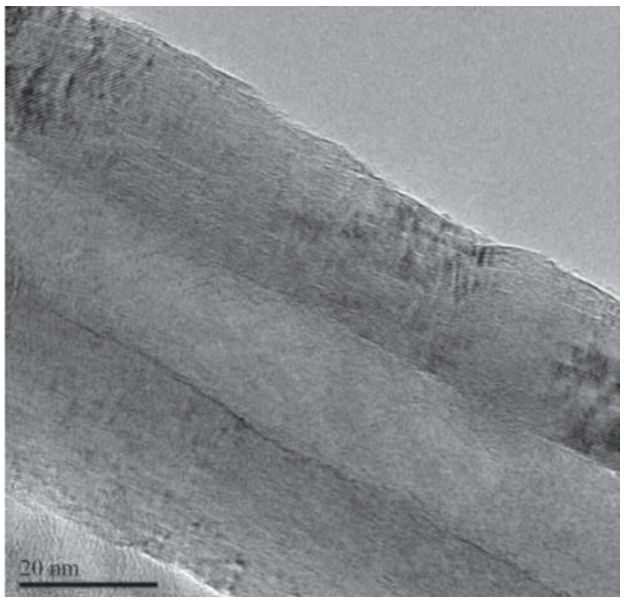

Figure 21 – TEM image showing that the filaments were hollow tubes

entire surface. Although it is known that the mass loss was generally localized (and not uniform), the calculation provided a means to 'normalize' the values by incorporating the exposure time and the exposed area of the sample (which will be more representative than purely a cumulative mass-loss value). By introducing the density, the penetration rate was calculated as follows:

Penetration rate (mm/a) = [87 600 x mass loss (g)] / [density (g/cm^3) x area (cm^2) x exposure time (hours)].

Figure 22 illustrates that Type 316L and 316Ti were significantly more attacked than the other grades. The stabilized grade initially performed better than the standard

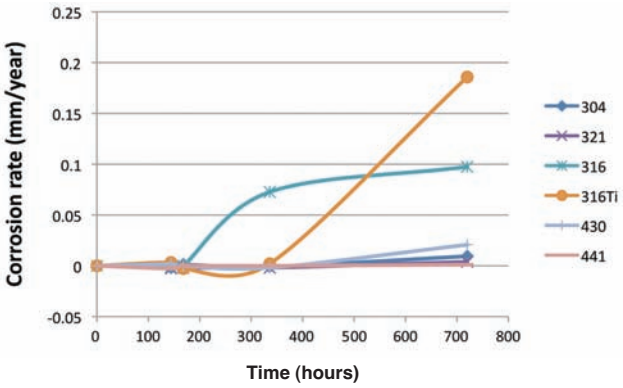

Figure 22—Corrosion rates of the samples tested over the test period

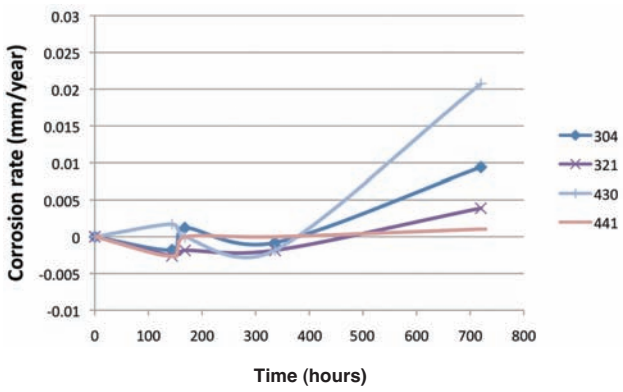

Figure 23—Corrosion rates of selected samples over the test period

Type 316L, although once the sample started to corrode, the rate was significantly higher. Figure 23 (with an expanded y-axis) shows the relative performance of the other alloys. Type 321 performed better than 304, and Type 441 performed better than 430.

Discussion

The Type 304L stainless steel performed well in the test, particularly compared to Type 316L, and revealed less metal wastage than the Type 321 sample. Although the mass-loss data indicate that Type 304L was attacked to a greater degree, cross-sections revealed greater attack in the Type 321 sample, where the corrosion products were also weighed and included as 'unaffected material'.

The Type 316L and 316Ti samples were attacked significantly more than all the other alloys. Initially, Type 316Ti performed better than the Type 316L sample, but once the corrosion started, the rate of attack was significantly greater than for the 316L sample. This could be due to the effect of the titanium that initially tied up the carbon to prevent carburization, and left chromium free to provide protection. However, these phases (refractory metal carbides) subsequently oxidized to increase the metal dusting rate significantly (Strauss and Grabke, 1998; Young, 2010). This effect could also explain the significant difference between the Type 304L and 316L samples. Apart from the addition of molybdenum in the 316L samples, the alloys were very similar. The carbides on the grain boundaries of the Type 316L material were enriched with chromium and molybdenum. Therefore, apart from resulting in de-alloyed chromium zones around the grain boundaries that were preferentially attacked, the expansion of the carbides upon subsequent oxidation resulted in mechanical stresses in the protective coating that caused breakage and allowed carbon ingress. The use of alloys containing molybdenum is therefore not recommended for use in metal dusting environments.

From the visual examination, as well as the mass-loss data, the ferritic grades (Types 430 and 441) performed better than the austenitic grades. The greater mobility of chromium in the ferritic material, compared to austenitic structures, helped to provide better resistance of the ferritic materials than the austenitics used (all with approximately the same chromium content). Areas associated with breaks in the oxide scale in both Type 430 and 441 had essentially no chromium to a depth of 200 µm to 300 µm, which was the radius from where chromium diffused to the surface to heal/repair the oxide. Although this effect provided greater resistance of the ferritic alloys to metal dusting in these tests for a period of 30 days, extended use will probably lead to rapid degradation as these zones will then behave similarly to carbon steel.

The importance of maintaining a passive oxide layer to prevent carbon deposition and diffusion into the metal was clearly demonstrated. The ferritic materials revealed significantly less coking compared to Type 316L and 316Ti. This was due to the ease with which chromium can diffuse through the ferritic matrix to heal breaks in the passive oxide layer, thereby preventing carbon deposition from the carbon-oversaturated gas mixture. The importance of a high chromium content (or addition of other elements like aluminium and/or silicon to promote a stable oxide layer), as well as a ferritic structure, are highlighted as possibilities to develop alloys to mitigate attack by metal dusting.

The advantage of using austenitic alloys to prevent metal dusting is that the carbon diffusion rate is slow. For the relative low nickel concentration ranges used in this study (8% to 10%), the austenite structure (which mitigates metal dusting by slowing the carbon diffusion rate) was not as effective as the advantage of an increased chromium diffusion rate provided in ferritic alloys. It must be noted that the exposure period of 30 days was relatively short, and an accelerated rate of attack for the ferritic alloys can be expected for longer exposure periods. The effect of slower carbon diffusion in the austenitic structure was therefore secondary to the effect of the greater mobility of the chromium in the ferritic structure in resisting metal dusting.

Alloys should also not contain any precipitates; since these provide sites for coke formation. The formation of secondary phases at elevated temperatures should also be avoided. These phases oxidize, and the resultant mechanical stresses cause breaks in the protective oxide layer, which allows carbon deposition and ingress (i.e. internal carburization).

The Type III mechanism was dominant in the alloys tested, i.e. selective oxidation of alloy carbides. The greater mobility of chromium in the ferritic materials promoted improved healing of the chromia scale, which prevented carbon deposition and ingress. The disintegration of the molybdenum-containing carbides caused a greater disruption in the chromia scale, which led to a greater degree of carbon ingress, and hence metal dusting, in the alloys containing molybdenum.

Conclusions

The ferritic materials performed better than the austenitic materials with similar chromium contents (18wt%). This was due to the greater mobility of chromium, which diffused towards the surface to heal breaks in the oxide layer. However, this resulted in essentially a layer of carbon steel on the outer surface that could increase the metal dusting rate significantly during prolonged use. This demonstrates the advantage that ferritic alloys offer, which could be explored by further improving the resistance of these alloys by the addition of other elements to provide a stable oxide film to prevent carbon ingress.

While carbide-forming elements (titanium and niobium) initially provided protection against metal dusting, the rate of attack increased subsequently. The initial superior performance is ascribed to the fact that these elements tie up the carbon ingress, leaving the chromium in the alloy free to protect the material. However, subsequent oxidation of these refractory metal carbides increased the rate of attack.

Type 316L performed significantly worse than Type 304L. Since molybdenum is also a carbide former, the effect is probably similar to that described above for titanium and niobium. Molybdenum alloys should therefore not be used in applications where metal dusting is a problem.

The selective oxidation of carbides (Type III mechanism) was the dominant mechanism of metal dusting in the alloys tested. The alloys containing more carbides (including titanium-, niobium-, and molybdenum carbides), degraded at higher rates.

Acknowledgments

This paper is published with the permission of Mintek. The assistance of Mintek, and Department of Science and Technology (DST) through the Advanced Metals Initiative (AMI) is gratefully acknowledged for funding, and Columbus Stainless for supplying material. Professor Lesley Cornish thanks the National Research Foundation for support.

References

Grabke, H.J. 1995. Metal dusting of low- and high-alloy steels. *Corrosion,* vol. 51, no. 9. pp. 711–720.

Grabke, H.J. 1998. Thermodynamics, mechanisms and kinetics of metal dusting. *Materials and Corrosion*, vol. 49. pp. 303–308.

Grabke, H.J., Krajak, R., and Müller-Lorenz, E.M. 1993. Metal dusting of high temperature alloys. *Werkstoffe und Korrosion*, vol. 44. pp. 89–97.

Hochman, R.F. and Burson, J.H. 1966. The fundamentals of metal dusting. *Proceedings of the American Petroleum Institute Division of Refining*, vol. 46. pp. 331–344.

Hochman, R.F. 1972. Basic studies of metal dusting deterioration in carbonaceous environments at elevated temperatures. *Proceedings of the. of the 4th International Congress on Metal Corrosion*, Amsterdam, The Netherlands. pp. 258–263.

Holland, M.L. 2012. Refinery damage mechanisms (based on API 571). Course presented to the Corrosion Institute of Southern Africa, Cape Town.

Hultgren, A. and Hillert, M. 1953. Conditions for the formation of cementite during carburizing of nickel steel (in Swedish). *Jernkont. Ann*, vol. 137, no. 7.

Lai, G.Y. 2007. High-Temperature Corrosion and Materials Applications. ASM International, Novelty. Ohio.

Nickel Development Institute. 2002. High-Temperature Characteristics of Stainless Steels, *Designers' Handbook*, Series, No. 9004.http://www.nickelinstitute.org/~/Media/Files/TechnicalLiterature/High_TemperatureCharacteristicsofStainlessSteel_9004_.pdf [Accessed 19 June 2012].

Pippel, E., Woltersdorf, J., Grabke H.J., and Strauss, S. 1995. Microprocesses of metal dusting on iron. *Steel Research*, vol. 66, no. 7. pp. 217–221.

Pippel, E., Woltersdorf, J., and Schneider, R. 1998. Micromechanisms of metal dusting on Fe-base and Ni-base alloys. *Materials and Corrosion*, vol. 49, no. 5. pp. 309–316.

Strauss, S. and Grabke, H.J. 1998. Role of alloying elements in steels on metal dusting. *Materials and Corrosion*, vol. 49. pp. 321–327.

Szakálos, P. and Liu, L. 2002. Mechanisms of metal dusting—Application to alloy composition, temperature and pressure. *15th International Corrosion Conference (ICC)*, Granada, September, 2002. Paper 806.

Szakálos, P. 2002. Mechanisms of metal dusting on stainless steels. Licentiate thesis, University of Stockholm, Sweden.

Szakálos, P. 2003. Mechanisms and driving forces of metal dusting. *Materials and Corrosion*, vol. 54, no. 10. pp. 752–762.

Szakálos, P. 2004. Mechanisms of metal dusting. PhD thesis, Royal Institute of Technology and Swedish Institute for Metals Research, Stockholm.

Szakálos, P. Pettersson, R., and Hertzman, S. 2002. An active corrosion mechanism for metal dusting on 304L stainless steel. *Corrosion Science*, vol. 44, no. 10. pp. 2253–2270.

Young, D.J. 2010. Carburisation and metal dusting. *Shreir's Corrosion*, 4th edn. Cottis, B., Graham, M., Lindsay, R., Lyon, S., Richardson, T., Scantlebury, D., and Stott, H. (eds.). Elsevier, Amsterdam. vol. 1, pp. 273–301.

Young, D.J., Zhang, J., Geers, C., and Shutze, M. 2011. Recent advances in understanding metal dusting: a review. *Materials and Corrosion*, vol. 62, no 1. pp. 7–28. ◆